reactions

MDPI

Communication

A New Nonaqueous Flow Battery with Extended Cycling

Diqing Yue [1,2], Weilin Zhang [3], Ivy Zhao [3], Xiaoting Fang [1,2], Yuyue Zhao [1], Jenny Li [1], Feng Zhao [3,*] and Xiaoliang Wei [1,*]

[1] Department of Mechanical and Energy Engineering, Indiana University-Purdue University Indianapolis, Indianapolis, IN 46202, USA
[2] School of Mechanical Engineering, Purdue University, West Lafayette, IN 47907, USA
[3] Storagenergy Technologies, Salt Lake City, UT 84104, USA
* Correspondence: fzhao@storagenergy.com (F.Z.); wei304@purdue.edu (X.W.); Tel.: +1-801-386-8555 (F.Z.); +1-317-274-8983 (X.W.)

Abstract: Nonaqueous flow batteries hold promise given their high cell voltage and energy density, but their performance is often plagued by the crossover of redox compounds. In this study, we used permselective lithium superionic conducting (LiSICON) ceramic membranes to enable reliable long-term use of organic redox molecules in nonaqueous flow cells. With different solvents on each side, enhanced cell voltages were obtained for a flow battery using viologen-based negolyte and TEMPO-based posolyte molecules. The thermoplastic assembly of the LiSICON membrane realized leakless cell sealing, thus overcoming the mechanical brittleness challenge. As a result, stable cycling was achieved in the flow cells, which showed good capacity retention over an extended test time.

Keywords: nonaqueous flow battery; organic; permselectivity; LiSICON; stability

Citation: Yue, D.; Zhang, W.; Zhao, I.; Fang, X.; Zhao, Y.; Li, J.; Zhao, F.; Wei, X. A New Nonaqueous Flow Battery with Extended Cycling. *Reactions* **2024**, *5*, 452–461. https://doi.org/10.3390/reactions5030023

Academic Editor: César Augusto Correia de Sequeira

Received: 17 June 2024
Revised: 24 July 2024
Accepted: 27 July 2024
Published: 28 July 2024

1. Introduction

Globally, renewable energies supply clean power as a pathway to accelerating decarbonization, but they are facing a critical challenge of intermittency. This drawback can eventually destabilize the power grid, which thus necessitates the integration of stationary energy storage systems. Flow batteries (FBs) are a promising long-duration storage approach, because the cell design enables the decoupling of energy and power, leading to convenient, independent scalability [1,2]. Redox-active components are key materials for achieving energy-dense, stable FBs. While aqueous FBs are being widely developed, nonaqueous FBs can provide an alternative solution regarding the need for high energy density by enabling higher cell voltages, despite the non-negligible challenge of their high electrolyte viscosity and resistivity [3]. Organic redox molecules are attractive candidates that are under intensive investigation in nonaqueous FBs [4–7]. Because of their structural diversity and tailorability, the solubility, redox potential, and stability of these compounds can be effectively enhanced. Representative organic redox scaffolds, such as ferrocene [8], TEMPO [9], dialkoxybenzene [10], phenothiazine [11], pyridinium [12], and cyclopropenium [13], have been structurally engineered to have desirable properties for use in nonaqueous FBs. However, despite their encouraging molecular properties, the long cycling of these molecules under FB-relevant conditions is rather limited. The lack of competitive cell performance has become one of the major concerns raised regarding nonaqueous FBs.

Among the various limiting factors, the chemical instability of redox molecules causes the loss of useful redox materials during cycling operations and thus has a direct impact on the cycle life of FBs. The charged states of organic molecules are often in the form of reactive ionic radicals, which may react with the electrolyte components or self-decompose to form side products [14–16]. Approaches to impart π conjugation or a steric barrier to the redox cores have been extensively explored to improve molecular stability [17–20].

Another technical challenge facing the use of nonaqueous FBs is the lack of suitable membranes with both permselectivity and ionic conductivity [21,22]. Porous separators have suitable conductivity but suffer from low permselectivity due to the large pore size of several tens to several hundreds of microns [23]. Ion exchange membranes, widely used in vanadium and other aqueous FBs [24,25], have also been considered for nonaqueous FBs but with limited success [26,27]. In general, nonaqueous electrolytes lack the "hydrating" environments needed to enable small-size ion transport channels and fast Grotthuss ion transport [28], which often result in significant drawbacks in terms of dimensional swelling, redox molecule crossover, or limited ionic conductivity. Therefore, achieving the long-term stable operation of nonaqueous flow cells, especially under high redox concentration conditions, requires the development of reliably performing redox molecules and membranes.

In this paper, we report a new nonaqueous FB system, with long cycling achieved with the use of chemically durable negolyte and posolyte organic molecules and a permselective lithium superionic conducting (LiSICON) membrane. Synthetic methyl viologen bis(trifluoromethane)sulfonimide (MV^{2+}-$TFSI_2$) and *N*,N,N-2,2,6,6-heptamethylpiperidinyloxy-4-ammonium bis(trifluoromethane)sulfonimide (TMA-TEMPO-TFSI) were used as the negolyte and posolyte molecules, respectively. The solvents used in the nonaqueous electrolytes were found to have significant effects on their solubility and redox potential, offering a viable method for maximizing the energy density for this FB system. Because of their dense ceramic structures, LiSICON membranes are known for their exclusive permselectivity for Li^+ ions over redox molecules and electrolyte solvents. This feature allows for the use of different solvents across the membrane and thus solvent-tailored high cell voltage. Under unoptimized conditions, the MV^{2+}-$TFSI_2$/TMA-TEMPO-TFSI flow cell demonstrated long-cycling behavior, maintaining a capacity retention of 99.79% per cycle and 99.5% per day throughout over a test period of 60 days.

2. Experimental Section

2.1. Materials and Methods

1,3-Propanesultone (≥99% GC), iodomethane (99+%), acetone (99.5%), and anhydrous N,N-dimethylformamide (DMF, 99.9%) were purchased from Fisher Scientific (Pittsburgh, PA, USA). 4-Amino-2,2,6,6-tetramethylpiperidine-1-oxyl (4-amino-TEMPO, 98%) 4,4′-bipyridine (98%), and lithium bis(trifluoromethane)sulfonimide (LiTFSI, 98%) were purchased from Ambeed (Arlington Heights, IL, USA). Bis(ethylcyclopentadienyl)cobalt(II) was purchased from Sigma-Aldrich (St. Louis, MO, USA). Battery-grade LiTFSI, acetonitrile (MeCN), 1,2-dimethoxyethane (DME), ethylene carbonate (EC), and ethyl methyl carbonate (EMC) were purchased from Gotion (Fremont, CA, USA). All chemicals were used as received, except DMF, which was dried over 3 Å molecular sieves for two days before use. Daramic® porous separators with a thickness of 175 microns were obtained from Daramic LLC (Owensboro, KY, USA).

The syntheses of the organic MV^{2+}-$TFSI_2$ and TMA-TEMPO-TFSI are described in Section S1 and Figures S1–S5 in the Supplementary Information. Also included is the preparation of the LiSICON membrane, which had a composition of $Li_{1.3}Al_{0.3}Ti_{1.7}(PO_4)_{3.0}$ (LATP).

^1H and ^{13}C nuclear magnetic resonance (NMR) spectra were obtained using a Bruker UltraShield 500MHz NMR spectrometer. Ultraviolet–visible (UV–vis) spectra were measured using a Thermo Scientific Evolution 600 UV–vis spectrometer. Field-emission scanning electron microscopy (FE-SEM) images were collected using a Joel JSM-7800F spectrometer. X-ray diffraction (XRD) spectra were collected using a Philips PANalytical X'Pert diffractometer with a thin-film detector. The surface area and particle size of LATP ceramic particles were measured using a Beckman Coulter LS230 laser diffraction particle size analyzer with a PIDS detector.

2.2. Cyclic Voltammetry (CV)

All electrochemical tests including CV and flow cells were carried out inside a Vigor® glove box (Houston, TX, USA) with the O_2 and H_2O levels below 1 ppm and at room temperature (i.e., 20 °C). A three-electrode cell was used with a 3 mm glassy carbon working electrode, a graphite felt strip counter electrode, and a $Ag/AgNO_3$ (10 mM Ag^+ in MeCN) reference electrode. The solutions used for CV measurements contained 10 mM redox molecules (MV^{2+}-$TFSI_2$ or TMA-TEMPO-TFSI) in the supporting electrolytes of 1 M LiTFSI in solvents. Different solvents including MeCN, DME, DMF, and EC-EMC (3:7 by weight) were used to investigate the effect on the redox potential. CV curves for a potential sweeping rate (v) ranging from 10 to 500 mV s^{-1} were collected using a CHI760D workstation (CH Instruments, Bee Cave, TX, USA) and were used to obtain the diffusion coefficient (D) and the electrochemical rate constant (k_0) of each redox species.

2.3. Crossover Test

The crossover test was carried out at room temperature inside a Vigor® glove box using an H-type diffusion cell. The electrolyte chamber on the redox molecule side contained 30 mL of 0.1 M TMA-TEMPO-TFSI in EC-EMC (3:7 by weight), and the blank chamber contained 30 mL of 0.1 M LiTFSI in EC-EMC (3:7 by weight). A 0.75″ diameter LATP disk was sandwiched between the two chambers. At specified time intervals, 3 mL aliquots of solution were extracted from the blank chamber and were subjected to CV measurements at a scan rate of 100 mV s^{-1}. The collected CV curves were compared to that of 10 mM TMA-TEMPO-TFSI in 0.1 M LiTFSI in EC-EMC (3:7 by weight) to confirm the occurrence of TMA-TEMPO-TFSI crossover. After completion of the CV test, the solutions were returned to the blank chamber.

2.4. Flow Cell Tests

A house-designed flow cell contained two directly stacked ELAT® carbon cloth electrodes (800 microns thick in total, Fuelcellstore, Bryan, TX, USA) on each side, a self-prepared LATP separator (1″ diameter), and expanded PTFE gaskets. The electrodes were punched into a circular shape with a diameter of 1.9 cm and an effective area of ~2.8 cm^2. These parts were thermally sealed with Surlyn® thermoplastic films (30 microns thick, Solaronix, Switzerland) at 100 °C in a vacuum oven for 2 h, followed by further sealing with Devcon® epoxy adhesive. The solutions used in the flow cell contained 7.5 mL of 20 mM MV^{2+}-$TFSI_2$ in EC-EMC (3:7 by weight) as the negolyte and 7.5 mL of 40 mM TMA-TEMPO-TFSI in DMF as the posolyte, respectively, both supported in 0.5 M LiTFSI. The electrolytes were circulated at a flow rate of 20 mL min^{-1} (i.e., an areal velocity of 2.2 cm s^{-1} at the maximum width of the circular electrode) using a Masterflex® L/S peristaltic pump. The flow cell was evaluated at a constant current density of 0.2 mA cm^{-2} using a BTS-5V50mA battery tester (Neware, Shenzheng, China).

The 0.2 M flow cell was tested using a larger-area flow cell with an interdigitated flow field design. An 8 × 8 cm LATP separator was thermoplastically sealed in the flow cell to obtain an effective area of 49 cm^2. The effect of flow rate was evaluated using electrochemical impedance spectroscopy (EIS). Then, the flow cell was loaded with 12 mL of 0.2 M MV^{2+}-$TFSI_2$ in EC-EMC (3:7 by weight) as the negolyte and 12 mL of 0.2 M TMA-TEMPO-TFSI in DMF as the posolyte, both supported by 0.5 M LiTFSI, which was tested under the same current density of 0.2 mA cm^{-2}.

3. Results and Discussion

Uses of TEMPO and dialkylated viologen in both aqueous and nonaqueous FBs are not rare, primarily because of the tailorability of their redox cores and the exceeding stability of their charged species [9,29–32]. In this study, the structural modification was aimed at achieving good solubilities in the organic solvents and maximizing the gap between redox potentials to achieve a high cell voltage. The $TFSI^-$ anion is well known to be compatible with common battery solvents and has been widely used to solubilize redox

molecules in nonaqueous electrolytes [8,33]. Thus, both molecular cores were structurally converted to bear quaternary ammonium cationic moieties and a $TFSI^-$ counterion. As shown in Scheme 1, MV^{2+}-$TFSI_2$ was synthesized at a high yield via a reaction between 4,4'-bipyridine and methyl iodide, followed by metathesis with LiTFSI to precipitate the product out of the aqueous medium. It is noted that the MV^{2+}-$TFSI_2$ was derived from the functional ingredient of a herbicide, paraquat, which is widely banned due to its high toxicity [34]; its application in large-scale energy storage may raise environmental concerns. To the TEMPO structure, a quaternary tetraalkylammonium group was introduced via reacting 4-amino-TEMPO with methyl iodide, and the following metathesis with LiTFSI yielded TMA-TEMPO-TFSI via precipitation. The electron-withdrawing ammonium group was designed to positively shift the redox potential of TEMPO and help enhance cell voltage.

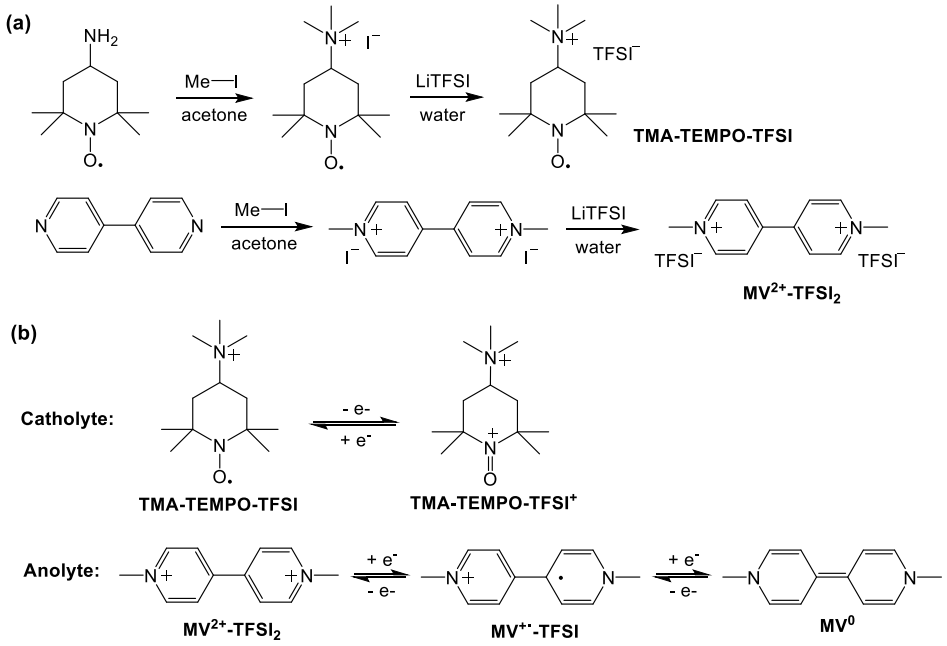

Scheme 1. (**a**) Synthesis of TMA-TEMPO-TFSI and MV^{2+}-$TFSI_2$; (**b**) electrochemical reactions of these two redox molecules.

Depending on the organic solvents used in nonaqueous FBs, organic redox molecules can have different solvation structures in the solution phase, which is expected to impact the solubilities and redox potentials [17,35]. The effects were investigated systematically by measuring the solubilities and cyclic voltammograms of these two compounds in a variety of commonly used battery solvents including MeCN, DME, EC-EMC (3:7), and DMF. The results are shown in Figure 1 and Table 1. The solubilities of TMA-TEMPO-TFSI were measured using UV–vis spectroscopy following Beer's law (Section S2, Figure S6). Due to the lack of a usable UV–vis absorption peak (Figure S7), the solubilities of MV^{2+}-$TFSI_2$ were obtained by measuring the densities of its solutions right at saturation (Section S2). MV^{2+}-$TFSI_2$ generally exhibited good solubilities of 0.90~1.36 M in these solvents. The solubility of TMA-TEMPO-TFSI showed a stronger solvent dependence ranging from <0.1 M in DME to 1.00 M in DMF. The solvents followed a consistent trend for both molecules in increasing their redox potentials in the order of EC-EMC, DME, DMF, to MeCN (Figure 1). Interestingly, MV^{2+}-$TFSI_2$ exhibited two reversible redox events in all solvents, which agrees with previous reports of MV analogs [32,33]. As expected, the quaternary ammonium favorably shifted the redox potential by +0.16 V compared to the plain TEMPO (Figure S8). When a LiSICON membrane was used, solvent cross-contamination was minimal, allowing different solvents to be used on both sides of the system to achieve higher cell voltages. For example, different combinations of solvents as the negolyte and posolyte tailored the cell voltage ranging from 0.85 V and 1.27 V to

1.75 V and 2.18 V for the first and second redox events, respectively. Therefore, the solvent effect can be used as an effective approach to increase the cell voltage and energy density of nonaqueous FBs. In addition, the electrochemical rate constants (k_0) of the two redox compounds were obtained from their cyclic voltammograms at a variety of scan rates using the Nicholson method (Section S3 and Figures S9–S16) [36]. As shown in Table 1, the rate constants of both compounds in all these solvents are comparable to those of most of the reported organic redox molecules [6,37]. To maximize the combined properties including solubility and redox potential, we chose EC-EMC as the solvent for MV^{2+}-$TFSI_2$ and DMF for TMA-TEMPO-TFSI in the ensuing flow cell tests.

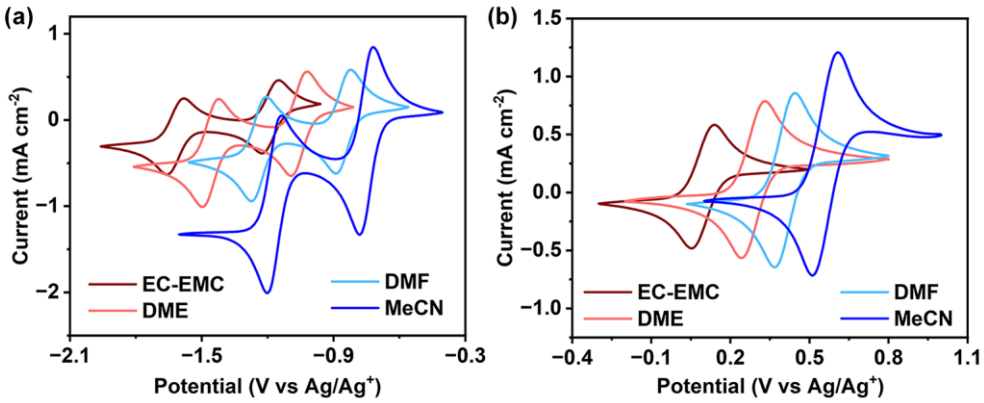

Figure 1. CV curves in different solvents: (**a**) 10 mM MV^{2+}-$TFSI_2$ and (**b**) 10 mM TMA-TEMPO-TFSI in 1 M LiTFSI. The scan rate was 20 mV s^{-1}.

Table 1. The measured solubilities, redox potentials E (V vs. Ag/Ag^+), diffusion coefficients (D in cm^2 s^{-1}), and kinetic constants (k_0 in cm s^{-1}) of MV^{2+}-$TFSI_2$ and TMA-TEMPO-TFSI in selected solvents.

Solvent	MV^{2+}-$TFSI_2$							TMA-TEMPO-TFSI			
	Solubility	E_1 [a]	D_1 [a]	$k_{0,1}$ [a]	E_2 [b]	D_2 [b]	$k_{0,2}$ [b]	Solubility	E	D	k_0
EC-EMC (3:7)	1.13 M	−1.62	1.18×10^{-6}	2.42×10^{-3}	−1.19	1.24×10^{-6}	2.00×10^{-3}	0.21 M	0.10	0.97×10^{-6}	1.46×10^{-3}
DME	0.90 M	−1.46	1.64×10^{-6}	1.64×10^{-3}	−1.06	2.16×10^{-6}	1.83×10^{-3}	<0.1 M	0.28	3.43×10^{-6}	2.92×10^{-3}
DMF	1.30 M	−1.24	2.71×10^{-6}	5.90×10^{-3}	−0.86	2.62×10^{-6}	5.04×10^{-3}	1.00 M	0.41	3.69×10^{-6}	5.14×10^{-3}
MeCN	1.36 M	−1.17	5.49×10^{-6}	6.58×10^{-3}	−0.75	5.50×10^{-6}	3.85×10^{-3}	0.55 M	0.56	5.89×10^{-6}	2.56×10^{-3}

[a] The first redox event; [b] the second redox event.

Limited permselectivity has become a well-recognized membrane challenge that prevents nonaqueous FBs from achieving long-term stable cycling. The irreversible crossover of redox molecules likely results in low efficiency, material contamination, unwanted cross-reactions, and/or expedited molecular decomposition. LiSICON-based ceramic separators are among the few membranes that exclude the through-membrane transport of redox molecules and organic solvents. The dense crystalline structures offer small mobility channels suitable only for Li^+ ions. LiSICON membranes have been used in nonaqueous FBs, but the majority of these tests were carried out under nonflow conditions [21,22]. The primary reason is that these membranes are mechanically brittle and lack sufficient shear strength to survive compressive cell-sealing. In a previous study, we demonstrated that the use of thermoplastic sealing [38] is highly effective for reliably assembling leak-free flow cells.

LATP powder was prepared via the solid-state reaction of raw materials, followed by high-energy ball-milling to break down the particle size (Figure S17a,b). The surface area of the ball-milled powder was determined to be 10.5 m^2 g^{-1} with a D50 of 2.6 μm, which is suitable for slurry preparation. The density of sintered LATP pellets made from this powder is usually 98% of the theoretical value. Green tapes were obtained from the

LATP slurry via the tape casting method (Figure S17c), laser cutting to the desired sizes, and calcination to produce LATP membranes (Figure S17d). As shown by the surface and cross-sectional SEM images in Figure 2, the ~300 µm thick LATP separator had a smooth surface and dense structures, which were beneficial for achieving permselective properties. To determine the crystal structure, the XRD pattern of the obtained LATP separator was compared with that with the standard diffraction peaks of the rhombohedral structure of the NASICON-type $LiTi_2(PO_4)_3$ of LATP ceramics (JPCDS No. 35-0754). The near-perfect match between them (Figure 2c) indicated the absence of crystalline impurities. Because of the good phase purity, a Li^+ conductivity as high as 1.9 ± 0.2 mS cm^{-1} was obtained in the LATP separator.

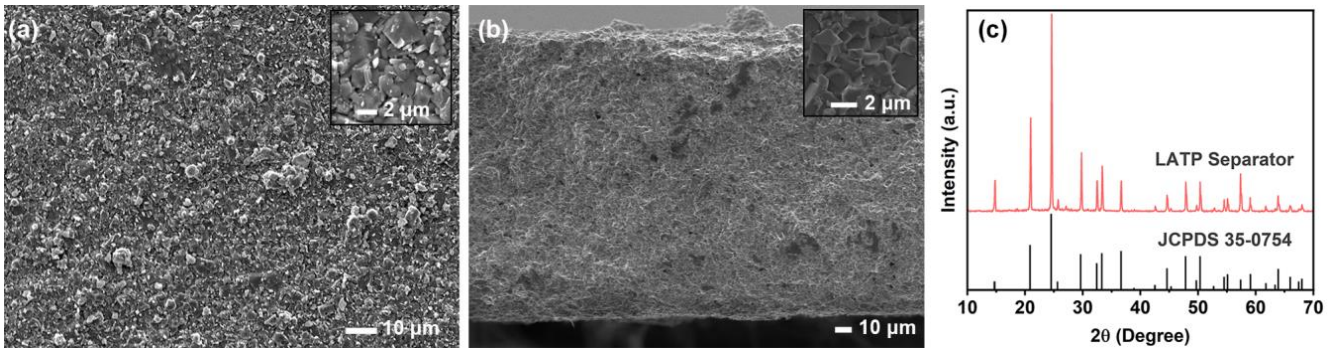

Figure 2. (**a**) Surface and (**b**) cross-sectional FE-SEM images of the LATP separator. Insets show expanded views. (**c**) XRD spectra of the obtained LATP separator as well as the standard diffraction peaks (JCPDS 35-0754).

An H-type diffusion cell was used to determine whether the crossover of organic redox molecules, e.g., TMA-TEMPO-TFSI used in this study, through the LATP membrane is possible (Figure 3a). The CV scans of the counter (blank) chamber electrolyte at a series of time intervals showed no sign of TMA-TEMPO-TFSI present, as well as negligible changes in the color and volume of the electrolytes on either side (Figure 3b). This was in sharp contrast to the porous separators. The use of a Daramic® porous separator under similar conditions resulted in fast coloration changes and volume decreases in the blank chamber electrolyte (Figure S18). This observation suggested the ability of LATP membrane to block the penetration of organic redox molecules and solvents. When used in flow cells, the crossover-free feature is expected to enable electrolyte retention and long-term cycling for chemically stable redox compounds.

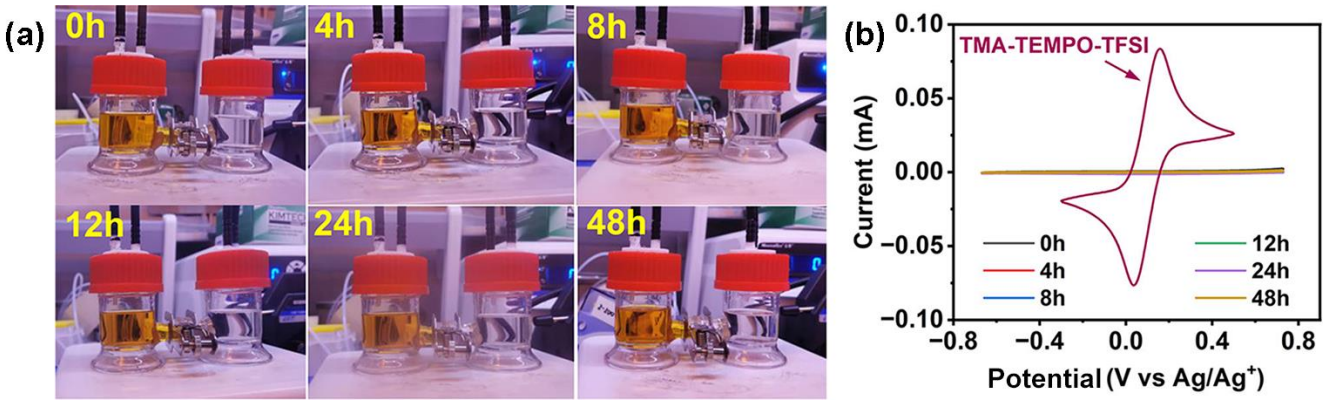

Figure 3. The crossover test result: (**a**) the H-type diffusion cell at different times; (**b**) the CV curves of the blank chamber electrolytes at different times compared to those of 10 mM TMA-TEMPO-TESI.

LATP membranes have been applied in nonaqueous flow cells, but the traditional compressive assembly method resulted in limited success [38–40]. Compared to mechani-

cally flexible polymeric membranes, the brittleness of thin ceramic membranes makes them vulnerable to compression forces perpendicular to their surfaces. Our LATP membranes failed to survive torque forces of >25 inch·pounds used for bolting the cell parts. Therefore, a different assembly method was evaluated. In this work, LATP membranes were thermoplastically assembled into nonaqueous flow cells of various sizes using Surlyn® thin-film sealants (Figure S19). This cell assembly method eliminated the traditional need for high compression forces, and we found that it achieved the strong leakless sealing of nonaqueous electrolytes for extended test periods. The biaxial fracture strength of these LATP membranes was measured as 123 ± 17 MPa (Section S4, Table S1 and Figure S20), in good agreement with this observation. The thermoplastically sealed cells were used to evaluate MV^{2+}-$TFSI_2$ and TMA-TEMPO-TFSI under flow conditions (Figure 4a). ELAT® carbon cloth electrodes show enhanced transport properties [41] and were used in our nonaqueous flow cells. In our initial test, low concentrations of redox molecules, e.g., 20 mM MV^{2+}-$TFSI_2$ in 0.5 M LiTFSI in EC-EMC as the negolyte and 40 mM TMA-TEMPO-TFSI in 0.5 M LiTFSI in DMF as the posolyte, were loaded to study the electrochemical properties. Electrochemical impedance spectroscopy (EIS) was used to measure the area-specific resistance (ASR) of the flow cell. Compared to the typical ohmic ASRs of 3~18 Ω cm^2 with porous separators [23], the significantly higher ohmic ASR of our flow cell, as shown in the Nyquist plot (37 Ω cm^2, Figure S21), indicated that the LATP membrane was the major contributor to the overall ASR. As a result, the flow cell could only be operated at low current densities such as 0.2 mA cm^{-2}, and limited performance was delivered at 1 mA cm^{-2} or above.

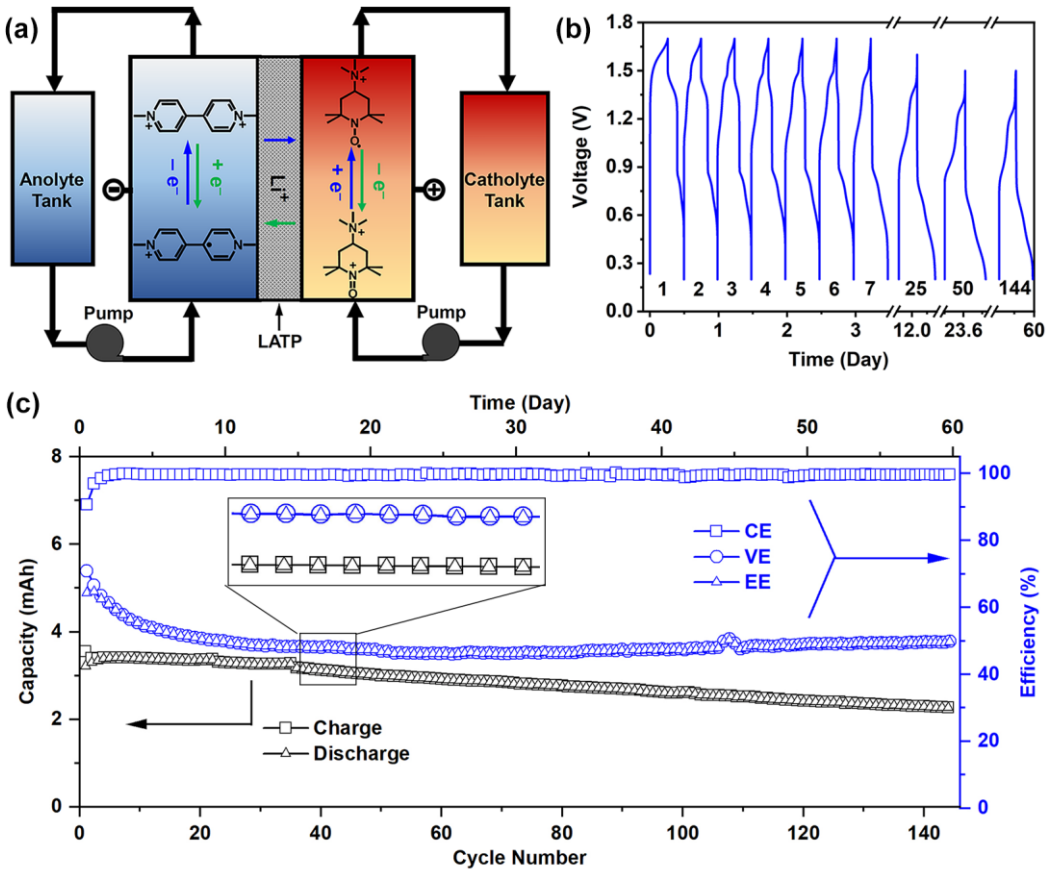

Figure 4. (**a**) Schematic illustration, (**b**) voltage curves, and (**c**) capacities and efficiencies of a LiSICON-based MV^{2+}-$TFSI_2$/TMA-TEMPO-TFSI flow cell using one electron. The numbers in panel (**b**) represent the number of cycles. The current density was 0.2 mA/cm^2. The negolyte was 20 mM MV^{2+}-$TFSI_2$ in 0.5 M LiTFSI/EC-EMC, and the posolyte was 40 mM TMA-TEMPO-TFSI in 0.5 M LiTFSI/DMF.

We attempted to utilize the $2e^-$ capacity of MV^{2+}-$TFSI_2$ by including the second voltage plateau during the cycling of a similar flow cell (Figure S22). Due to the low current density (0.2 mA cm^{-2}), the first charge/discharge cycle corresponded to 11.3 h. However, a fast capacity fading was observed together with the rapid reduction in the upper plateau, indicating the fully charged species MV^0 lacked sufficient long-term chemical stability in the nonaqueous electrolyte. On the contrary, access only to the first redox activity of MV^{2+}-$TFSI_2$ led to exceeding cycling stability. Figure 4b,c show the voltage curves of the selected cycles, cycling capacities, and efficiencies of the flow cell. Stable coulombic efficiency (CE) was maintained throughout 145 cycles, with an average value of 99.5%. The voltage efficiency (VE) and energy efficiency (EE) gradually dropped from ~70% to ~50% during the first 20 cycles and then stabilized at around 50%. The initial capacity represented a material utilization ratio of 89%. The flow cell lost 30% of its initial capacity over the 145 cycles (~60 days), corresponding to an average capacity fading rate of 0.21% per cycle and 0.5% per day. In a separate flow cell under similar conditions, relatively stable cycling was also observed over a month-long test time, albeit with a slightly different capacity profile (Figure S23a,b). The capacity decreased during the first 20 cycles and then stabilized for an additional 65 cycles, resulting in an average capacity fading of 0.41% per cycle. Postcycling CV analysis detected no formation of new redox peaks (Figure S23c,d), suggesting the high stability of the two redox molecules. The capacity retention demonstrated in our flow cells is among the best cycling performances reported for nonaqueous FBs. In addition, the long cyclability reflects the reliability of the thermoplastic sealing that enables the durable, leak-free assembly of LiSICON-based membranes into nonaqueous flow cells.

Surprisingly, the voltage curves of the flow cells exhibited unexpected behavior (Figure 4b). The flow cell started with a single voltage plateau in the first charging process, indicating a $1e^-$ reaction, but more than one voltage plateau was commonly observed in the following operations. Additionally, as the cycling proceeded, the voltage curve not only showed plateau-vanishing but also experienced an overall drop. These voltage behaviors repeatedly occurred in our flow cell tests (Figures S22–S24) but the underlying mechanisms are not well understood. A possible reason could be that the Ti^{4+} ions in the LATP membrane were reduced to Ti^{3+}, turning the negolyte-facing side into a light brown color (Figure S25). This chemical change in the LATP composition may have complicated the transport or reaction processes that occurred in the flow cells and modulated their voltage behaviors.

4. Conclusions

In conclusion, we achieved extended cycling in a new nonaqueous FB system exploiting chemically stable organic redox molecules and permselective LiSICON separators. The nature of the battery solvent controls the redox potentials of redox molecules, offering an effective approach for increasing cell voltage. Use of the absolute Li^+-selective LiSICON membrane effectively prevented the cross-contamination of the negolyte and posolyte by physically blocking the crossover of both redox molecules and battery solvents. The thermoplastic leakless assembly of LiSICON membranes circumvents the need for the traditional compressive sealing, providing a reliable method to extend the cycling of nonaqueous flow cells. Despite the low operational current density, the MV^{2+}-$TFSI_2$/TMA-TEMPO-TFSI flow cells showed exceptional cyclability over a test period of months. Our study addressed an important but underinvestigated area in nonaqueous FBs, and our method can serve as a universal test platform for the reliable study of nonaqueous redox chemistry under flow cell conditions.

Supplementary Materials: The following supporting information can be downloaded at: https://www.mdpi.com/article/10.3390/reactions5030023/s1, Section S1: Synthesis of organic redox molecules and LATP membranes; Section S2: Solubility measurement; Section S3: Determination of redox kinetics [36,42]; Section S4: Measurement of biaxial strength [43,44]; Section S5: Supporting figures.

Author Contributions: Conceptualization, F.Z. and X.W.; methodology, D.Y., and W.Z.; formal analysis, D.Y., W.Z., and X.W.; investigation, D.Y., W.Z., I.Z., X.F., Y.Z., and J.L.; data curation, X.W.; writing—original draft preparation, X.W.; writing—review and editing, D.Y., W.Z., Y.Z., and F.Z.; visualization, D.Y., X.W., and W.Z.; supervision, F.Z. and X.W.; project administration, F.Z. and X.W.; funding acquisition, F.Z. and X.W. All authors have read and agreed to the published version of the manuscript.

Funding: This work was financially supported by the U.S. Department of Energy, Office of Science, Small Business Innovation Research (award No. 077040-00002B) and by the U.S. National Science Foundation (award No. CHE-2055222).

Data Availability Statement: The data that support the conclusion of this work are available upon reasonable request.

Conflicts of Interest: The authors declare no conflicts of interest.

References

1. Dunn, B.; Kamath, H.; Tarascon, J.M. Electrical Energy Storage for the Grid: A Battery of Choices. *Science* **2011**, *334*, 928–935. [CrossRef]
2. Yang, Z.G.; Zhang, J.L.; Kintner-Meyer, M.C.W.; Lu, X.C.; Choi, D.W.; Lemmon, J.P.; Liu, J. Electrochemical Energy Storage for Green Grid. *Chem. Rev.* **2011**, *111*, 3577–3613. [CrossRef] [PubMed]
3. Gong, K.; Fang, Q.R.; Gu, S.; Li, S.F.Y.; Yan, Y.S. Nonaqueous redox-flow batteries: Organic solvents, supporting electrolytes, and redox pairs. *Energ. Environ. Sci.* **2015**, *8*, 3515–3530. [CrossRef]
4. Winsberg, J.; Hagemann, T.; Janoschka, T.; Hager, M.D.; Schubert, U.S. Redox-Flow Batteries: From Metals to Organic Redox-Active Materials. *Angew. Chem. Int. Ed.* **2017**, *56*, 686–711. [CrossRef]
5. Luo, J.A.; Hu, B.; Hu, M.W.; Zhao, Y.; Liu, T.L. Status and Prospects of Organic Redox Flow Batteries toward Sustainable Energy Storage. *Acs Energy Lett.* **2019**, *4*, 2220–2240. [CrossRef]
6. Cao, J.Y.; Tian, J.Y.; Xu, J.; Wang, Y.G. Organic Flow Batteries: Recent Progress and Perspectives. *Energ. Fuel* **2020**, *34*, 13384–13411. [CrossRef]
7. Li, M.; Rhodes, Z.; Cabrera-Pardo, J.R.; Minteer, S.D. Recent advancements in rational design of non-aqueous organic redox flow batteries. *Sustain. Energ. Fuels* **2020**, *4*, 4370–4389. [CrossRef]
8. Wei, X.L.; Cosimbescu, L.; Xu, W.; Hu, J.Z.; Vijayakumar, M.; Feng, J.; Hu, M.Y.; Deng, X.C.; Xiao, J.; Liu, J.; et al. Towards High-Performance Nonaqueous Redox Flow Electrolyte Via Ionic Modification of Active Species. *Adv. Energy Mater.* **2015**, *5*, 1400678. [CrossRef]
9. Wei, X.; Xu, W.; Vijayakumar, M.; Cosimbescu, L.; Liu, T.; Sprenkle, V.; Wang, W. TEMPO-Based Catholyte for High-Energy Density Nonaqueous Redox Flow Batteries. *Adv. Mater.* **2014**, *26*, 7649–7653. [CrossRef]
10. Huang, J.H.; Cheng, L.; Assary, R.S.; Wang, P.Q.; Xue, Z.; Burrell, A.K.; Curtiss, L.A.; Zhang, L. Liquid Catholyte Molecules for Nonaqueous Redox Flow Batteries. *Adv. Energy Mater.* **2015**, *5*, 1401782. [CrossRef]
11. Milshtein, J.D.; Kaur, A.P.; Casselman, M.D.; Kowalski, J.A.; Modekrutti, S.; Zhang, P.L.; Attanayake, N.H.; Elliott, C.F.; Parkin, S.R.; Risko, C.; et al. High current density, long duration cycling of soluble organic active species for non-aqueous redox flow batteries. *Energ. Environ. Sci.* **2016**, *9*, 3531–3543. [CrossRef]
12. Sevov, C.S.; Hickey, D.P.; Cook, M.E.; Robinson, S.G.; Barnett, S.; Minteer, S.D.; Sigman, M.S.; Sanford, M.S. Physical Organic Approach to Persistent, Cyclable, Low-Potential Electrolytes for Flow Battery Applications. *J. Am. Chem. Soc.* **2017**, *138*, 2924–2927. [CrossRef] [PubMed]
13. Sevov, C.S.; Samaroo, S.K.; Sanford, M.S. Cyclopropenium Salts as Cyclable, High-Potential Catholytes in Nonaqueous Media. *Adv. Energy Mater.* **2017**, *7*, 1602027. [CrossRef]
14. Zhang, J.J.; Slikrob, I.A.; Assary, R.S.; Tung, S.O.; Silcox, B.; Curtiss, L.A.; Thompson, L.; Zhang, L. Toward Improved Catholyte Materials for Redox Flow Batteries: What Controls Chemical Stability of Persistent Radical Cations? *J. Phys. Chem. C* **2017**, *121*, 23347–23358. [CrossRef]
15. Zhang, J.J.; Huang, J.H.; Robertson, L.A.; Assary, R.S.; Shkrob, I.A.; Zhang, L. Elucidating Factors Controlling Long-Term Stability of Radical Anions for Negative Charge Storage in Nonaqueous Redox Flow Batteries. *J. Phys. Chem. C* **2018**, *122*, 8116–8127. [CrossRef]
16. Wei, X.L.; Xu, W.; Huang, J.H.; Zhang, L.; Walter, E.; Lawrence, C.; Vijayakumar, M.; Henderson, W.A.; Liu, T.B.; Cosimbescu, L.; et al. Radical Compatibility with Nonaqueous Electrolytes and Its Impact on an All-Organic Redox Flow Battery. *Angew. Chem. Int. Ed.* **2015**, *54*, 8684–8687. [CrossRef] [PubMed]
17. Zhang, L.Y.; Qian, Y.M.; Feng, R.Z.; Ding, Y.; Zu, X.H.; Zhang, C.K.; Guo, X.L.; Wang, W.; Yu, G.H. Reversible redox chemistry in azobenzene-based organic molecules for high-capacity and long-life nonaqueous redox flow batteries. *Nat. Commun.* **2020**, *11*, 3843. [CrossRef] [PubMed]

18. Kowalski, J.A.; Casselman, M.D.; Kaur, A.P.; Milshtein, J.D.; Elliott, C.F.; Modekrutti, S.; Attanayake, N.H.; Zhang, N.J.; Parkin, S.R.; Risko, C.; et al. A stable two-electron-donating phenothiazine for application in nonaqueous redox flow batteries. *J. Mater. Chem. A* **2017**, *5*, 24371–24379. [CrossRef]
19. Walser-Kuntz, R.; Yan, Y.C.; Sigman, M.; Sanford, M.S. A Physical Organic Chemistry Approach to Developing Cyclopropenium-Based Energy Storage Materials for Redox Flow Batteries. *Accounts Chem. Res.* **2023**, *56*, 1239–1250. [CrossRef]
20. Duan, W.T.; Vemuri, R.S.; Milshtein, J.D.; Laramie, S.; Dmello, R.D.; Huang, J.H.; Zhang, L.; Hu, D.H.; Vijayakumar, M.; Wang, W.; et al. A symmetric organic-based nonaqueous redox flow battery and its state of charge diagnostics by FTIR. *J. Mater. Chem. A* **2016**, *4*, 5448–5456. [CrossRef]
21. Yuan, J.S.; Pan, Z.Z.; Jin, Y.; Qiu, Q.Y.; Zhang, C.J.; Zhao, Y.C.; Li, Y.D. Membranes in non-aqueous redox flow battery: A review. *J. Power Sources* **2021**, *500*, 229983. [CrossRef]
22. Lehmann, M.L.; Tyler, L.; Self, E.C.; Yang, G.; Nanda, J.; Saito, T. Membrane design for non-aqueous redox flow batteries: Current status and path forward. *Chem* **2022**, *8*, 1611–1636. [CrossRef]
23. Wei, X.L.; Duan, W.T.; Huang, J.H.; Zhang, L.; Li, B.; Reed, D.; Xu, W.; Sprenkle, V.; Wang, W. A High-Current, Stable Nonaqueous Organic Redox Flow Battery. *Acs Energy Lett.* **2016**, *1*, 705–711. [CrossRef]
24. Che, X.F.; Zhao, H.; Ren, X.R.; Zhang, D.H.; Wei, H.; Liu, J.G.; Zhang, X.; Yang, J.S. Porous polybenzimidazole membranes with high ion selectivity for the vanadium redox flow battery. *J. Membrane Sci.* **2020**, *611*, 118359. [CrossRef]
25. Che, X.F.; Tang, W.Q.; Dong, J.H.; Aili, D.; Yang, J.S. Anion exchange membranes based on long side-chain quaternary ammonium-functionalized poly(arylene piperidinium)s for vanadium redox flow batteries. *Sci. China Mater.* **2022**, *65*, 683–694. [CrossRef]
26. Pahari, S.K.; Gokoglan, T.C.; Chaurasia, S.; Bolibok, J.N.; Golen, J.A.; Agar, E.; Cappillino, P.J. Toward High-Performance Nonaqueous Redox Flow Batteries through Electrolyte Design. *ACS Appl. Energ. Mater.* **2023**, *6*, 7521–7534. [CrossRef]
27. Zhen, Y.H.; Zhang, C.J.; Yuan, J.S.; Zhao, Y.C.; Li, Y.D. A high-performance all-iron non-aqueous redox flow battery. *J. Power Sources* **2020**, *445*, 227331. [CrossRef]
28. Paddison, S.J.; Paul, R. The nature of proton transport in fully hydrated Nafion®. *Phys. Chem. Chem. Phys.* **2002**, *4*, 1158–1163. [CrossRef]
29. Liu, T.B.; Wei, X.L.; Nie, Z.M.; Sprenkle, V.; Wang, W. A Total Organic Aqueous Redox Flow Battery Employing a Low Cost and Sustainable Methyl Viologen Anolyte and 4-HO-TEMPO Catholyte. *Adv. Energy Mater.* **2016**, *6*, 1501449. [CrossRef]
30. DeBruler, C.; Hu, B.; Moss, J.; Liu, X.A.; Luo, J.A.; Sun, Y.J.; Liu, T.L. Designer Two-Electron Storage Viologen Anolyte Materials for Neutral Aqueous Organic Redox Flow Batteries. *Chem* **2017**, *3*, 961–978. [CrossRef]
31. Liu, Y.H.; Goulet, M.A.; Tong, L.C.; Liu, Y.Z.; Ji, Y.L.; Wu, L.; Gordon, R.G.; Aziz, M.J.; Yang, Z.J.; Xu, T.W. A Long-Lifetime All-Organic Aqueous Flow Battery Utilizing TMAP-TEMPO Radical. *Chem* **2019**, *5*, 1861–1870. [CrossRef]
32. Hu, B.; Liu, T.L. Two electron utilization of methyl viologen anolyte in nonaqueous organic redox flow battery. *J. Energy Chem.* **2018**, *27*, 1326–1332. [CrossRef]
33. Attanayake, N.H.; Liang, Z.M.; Wang, Y.L.; Kaur, A.P.; Parkin, S.R.; Mobley, J.K.; Ewoldt, R.H.; Landon, J.; Odom, S.A. Dual function organic active materials for nonaqueous redox flow batteries. *Mater. Adv.* **2021**, *2*, 1390–1401. [CrossRef]
34. Kim, J.W.; Kim, D.S. Paraquat: Toxicology and impacts of its ban on human health and agriculture. *Weed Sci.* **2020**, *68*, 208–213. [CrossRef]
35. Wang, X.; Xing, X.Q.; Huo, Y.J.; Zhao, Y.C.; Li, Y.D. A systematic study of the co-solvent effect for an all-organic redox flow battery. *Rsc Adv.* **2018**, *8*, 24422–24427. [CrossRef] [PubMed]
36. Wang, H.; Sayed, S.Y.; Luber, E.J.; Olsen, B.C.; Shirurkar, S.M.; Venkatakrishnan, S.; Tefashe, U.M.; Farquhar, A.K.; Smotkin, E.S.; McCreery, R.L.; et al. Redox Flow Batteries: How to Determine Electrochemical Kinetic Parameters. *Acs Nano* **2020**, *14*, 2575–2584. [CrossRef] [PubMed]
37. Wei, X.L.; Pan, W.X.; Duan, W.T.; Hollas, A.; Yang, Z.; Li, B.; Nie, Z.M.; Liu, J.; Reed, D.; Wang, W.; et al. Materials and Systems for Organic Redox Flow Batteries: Status and Challenges. *ACS Energy Lett.* **2017**, *2*, 2187–2204. [CrossRef]
38. Ding, Y.; Zhao, Y.; Li, Y.; Goodenough, J.B.; Yu, G. A high-performance all-metallocene-based, non-aqueous redox flow battery. *Energ. Environ. Sci.* **2017**, *10*, 491–497. [CrossRef]
39. Zhao, Y.; Byon, H.R. High-Performance Lithium-Iodine Flow Battery. *Adv. Energy Mater.* **2013**, *3*, 1630–1635. [CrossRef]
40. Chen, M.; Chen, H. High-capacity polysulfide–polyiodide nonaqueous redox flow batteries with a ceramic membrane. *Nanoscale Adv.* **2023**, *5*, 435–442. [CrossRef]
41. Forner-Cuenca, A.; Penn, E.E.; Oliveira, A.M.; Brushett, F.R. Exploring the role of electrode microstructure on the performance of non-aqueous redox flow batteries. *J. Electrochem. Soc.* **2019**, *166*, A2230–A2241. [CrossRef]
42. Compton, R.G.; Banks, C.E. *Understanding Voltammetry*; World Scientific: Singapore, 2018.
43. *ASTMC1499-09*; Standard Test Method for Monotonic Equibiaxial Flexure Strength of Advanced Ceramics at Ambient Temperature. ASTM: Philadelphia, PA, USA, 2009.
44. Weibull, W. A statistical distribution function of wide applicability. *J. Appl. Mech.* **1951**, *18*, 293–297. [CrossRef]